X-ray Diffraction of Ramp-Compressed Silicon to 390 GPa

X. Gong,^{1,2,*} D. N. Polsin,^{1,2} R. Paul,^{1,2} B. J. Henderson,^{1,3} J. H. Eggert,⁴ F. Coppari,⁴ R. F. Smith,⁴ J. R. Rygg,^{1,2,3} and G. W. Collins^{1,2,3}

University of Rochester Laboratory for Laser Energetics, Rochester, New York 14623-1299, USA
 Department of Mechanical Engineering, University of Rochester, Rochester, New York 14627-0132, USA
 Department of Physics and Astronomy, University of Rochester, Rochester, New York 14627-0171, USA
 Lawrence Livermore National Laboratory, Livermore, California 94550-9234, USA
 (Dated: January 20, 2023)

Silicon (Si) exhibits a rich collection of phase transitions under ambient-temperature isothermal and shock compression. This report describes *in-situ* diffraction measurements of ramp compressed Si between 40 and 389 GPa. Angle-dispersive x-ray scattering reveals that Si assumes an hexagonal close-packed (hcp) structure between 40 and 93 GPa, and, at higher pressure, a face-centered cubic (fcc) structure which persists to at least 389 GPa, the highest pressure for which the crystal structure of Si has been investigated. The range of hcp stability extends to higher pressures and temperatures than predicted by theory.

Si is one of the most abundant elements on Earth, and has been studied extensively at extreme conditions. X-ray diffraction on isothermally-compressed Si at room temperature using diamond anvil cell (DAC) technique reveals seven different structural phases, and four more during decompression [1]. Starting at ambient conditions, Si has a diamond cubic type structure (cd, Si-I, space group $Fd\overline{3}m$) [2], transitioning to Si-II (a β tin type, body-centered tetragonal (bct) structure, space group $I4_1/amd$) [3], Si-XI (an orthorhombic structure, space group Imma) [4, 5], Si-V (simple hexagonal structure, or sh, space group P6/mmm) [6], Si-VI (another orthorhombic structure, space group Cmce) [7], Si-VII (a hexagonal close-packed structure, or hcp, space group $P6_3/mmc$) [6], and finally Si-X (a face-centered cubic structure, or fcc, space group $Fm\overline{3}m$) [8], which remains stable to at least 248 GPa [9]. Anzellini et al. made the most recent systematic study of the phase boundaries by compressing Si more hydrostatically using helium as a pressure-transmitting medium [1].

Dynamic compression (shock, multishock, and ramp compression) experiments uniaxially load the sample and then the sample relaxes towards a more hydrostatic compression with time. Shock experiments have explored a variety of phase transitions in Si to 54 GPa [10–16]. Such transitions are usually inferred from wave splittings in the measured particle velocity data [10–13] due to violation of the stability condition, $\partial^2 p/\partial \rho^2 > 0$, on the shock Hugoniot near the phase boundary. More recently, in-situ x-ray diffraction was used to study solid-solid phase transitions and shock-induced melting of Si [14–16]. McBride et al. [14] observed a lowering of the cd- β tin-Imma phase boundary under shock compression. Turneaure et al. [16] observed that the sh structure coexists with the liquid along the melting curve above 30 GPa, before Si completely melts at around 33 GPa. Completely melted Si samples recrystallize into the hcp structure under reshock for shocked states below 36.7 GPa.

Recent first-principle simulations using density func-

tional theory (DFT) also provide important insight into the high-pressure and high-temperature phase diagram of Si [17–19]. Li et al. predict that at ambient temperature, the sh structure transforms into a double-hexagonal close-packed (dhcp, space group $P6_3/mmc$) structure at 33 GPa before it transforms into hcp structure at 41 GPa [17]. The predicted dhcp structure has not been observed by ambient temperature experiments [1]. Paul et al. [18, 19] also predicts the dhcp structure, albeit only above ambient temperature, and the principal isentrope crosses the Cmce-dhcp boundary at 22 GPa, the dhcp-fcc boundary at 55 GPa, after which the fcc structure is stable to 2.8 TPa. All such calculations were performed assuming hydrostatic compression.

Single-shock experiments access only a limited part of the solid Si phase space due to the large temperature increase and subsequent melting upon shock compression beyond 33 GPa [16]. In contrast, ramp compression, by gradually increasing the pressure load on the sample, can achieve high pressure states along a path bounded by the principal isentrope and the principal Hugoniot. The work described here used ramp compression techniques to explore the structural evolution with pressure of solid Si to several hundred GPa (several Mbar).

The experiments were performed on the OMEGA EP laser at the Laboratory for Laser Energetics, University of Rochester. The experimental configuration uses the powder x-ray diffraction image plates (PXRDIP) diagnostic [20] (Figure 1). The laser beam has an incident angle of 22.5° with respect to the target normal and a 1100-µm-diameter spot size with a super-Gaussian profile produced by distributed phase plates. The Si sample is $\langle 100 \rangle$ -oriented, single crystal, 10- to 22-µm-thick, and is sandwiched between plates of $\langle 110 \rangle$ -oriented, single crystal, 20- to 30-µm-thick diamond ablator, and a $\langle 100 \rangle$ -oriented, single crystal, 100- to 120-µm-thick LiF window. The pieces are held together by epoxy that is approximately 1- to 2-µm-thick. The target stack is mounted on a 75-µm-thick W, Ta or Pt plate with a 300-

or 400-µm-diameter pinhole aperture.

Ramp compression is accomplished by ablating the diamond with a laser pulse which gradually increases with power over 10 or 20 ns (Figure 1), creating a ramped compression wave that propagates through the target assembly. The impedance difference between these materials causes the ramped compression wave to reverberate within the Si layer as it is compressed to high pressure. The complete Si-LiF interface velocity history is accurately recorded to constrain this complex compression path.

When the Si sample achieves its peak compression, a backlighter foil (Cu or Ge) is illuminated with an 1-ns laser pulse to generate the x-rays used for diffraction. The laser irradiance is chosen to optimize x-ray conversion efficiency of Cu He- α (1.4816 Å) and Ge He- α (1.2097 Å) [21]. The x-rays are collimated by the pinhole, and diffract from both the compressed Si sample and the edge of the pinhole. The diffracted x-rays are filtered by Cu (or Al) and black kapton sheets and are recorded by image plates lining the PXRDIP box. The pinhole is not compressed at the time of x-ray illumination and is used to calibrate the geometry of diffraction experiments. The ambient crystal structures of W, Ta, and Pt are bcc, bcc, and fcc, respectively.

A line-imaging velocity interferometer system for any reflector (VISAR) [22] detects the Doppler shifts of a 532nm probe beam reflected off Si-LiF interface to measure the interface velocity as a function of time. The measured apparent velocity is corrected to account for the refractive index change of LiF due to compression [23]. The method of characteristics [24, 25] is used to determine the pressure distribution of the sample, with the interface velocity as the boundary condition. HYADES hydrodynamic simulations [26] are used to corroborate the results of the method of characteristics [27]. A Monte-Carlo (MC) algorithm is used to estimate the mean pressure and its standard deviation, accounting for the uncertainties of velocity due to VISAR record [22], LiF refractive index [23], sample layer thickness, Si initial density [16], LiF initial density [28], and LiF equation of state [23]. We also record the 1σ interval of the pressure distribution during the 1-ns x-ray exposure, averaged over the MC samples, to characterize pressure nonuniformity.

The x-ray image plates are projected onto $2\theta - \phi$ plane, where 2θ is the scattering angle and ϕ is the azimuthal angle around the direct x-ray direction (Figure 2). In this plane, Debye-Scherrer rings are projected into constant 2θ lines. A non-linear iterative peak-clipping (SNIP) algorithm is used to estimate and subtract the spatially slowly varying background [29]. Other features not originating from the compressed Si sample or pinhole substrate are masked out when taking the lineout of images (see supplementary material). The pinhole diffraction peaks are used for geometry calibration to accurately locate the diffraction scattering angles 2θ . A systematic

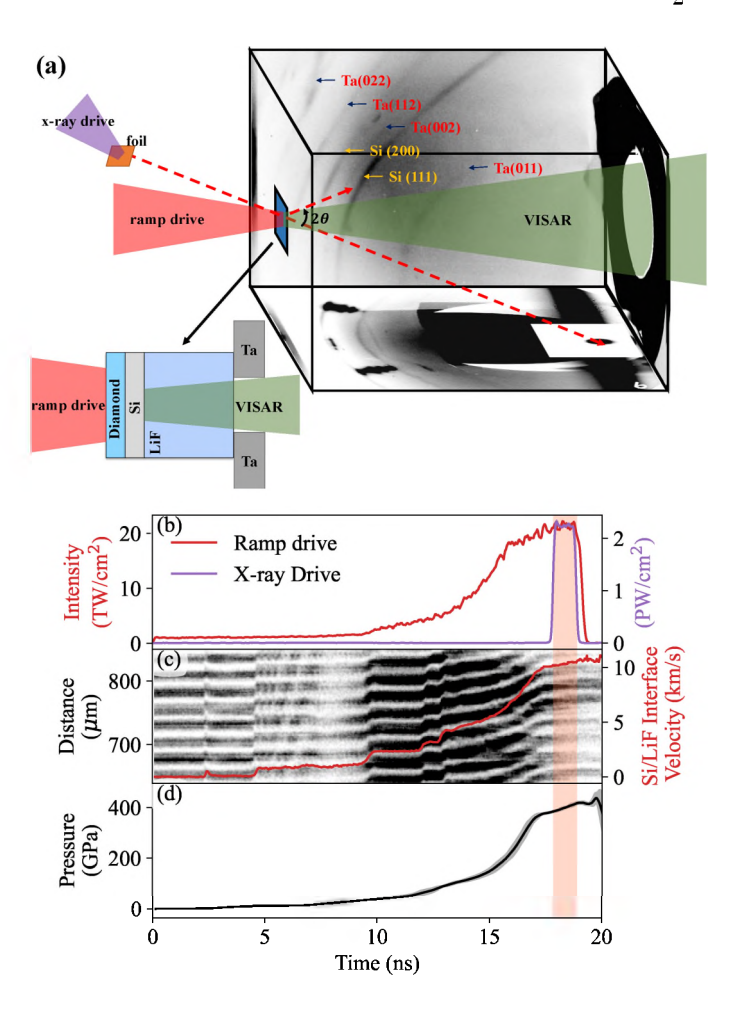


FIG. 1. (a) The PXRDIP experimental platform and diffraction data for shot 29637. A Si sample sandwiched between diamond ablator and lithium fluoride window is compressed with a 10- or 20-ns ramp laser pulse. Near peak compression, 1-ns laser pulse illuminates a Cu or Ge foil to produce He- α x-rays, which diffract from the compressed sample and are recorded by image plates lining the PXRDIP box. VISAR is used to record the Si-LiF interface velocity throughout the compression. (b) The delivered ramp laser pulse (red) and the 1-ns square laser pulse used to produce the x-ray source (purple) for shot 29637. (c) The VISAR streak image and the extracted apparent Si-LiF interface velocities for shot 29637. (d) Average Si pressure and its standard deviation for shot 29637 determined by the method of characteristics.

correction to 2θ is made to account for the fact that the pinhole substrate is slightly displaced from the sample [29].

Two distinct x-ray diffraction patterns from Si are observed between 40 and 389 GPa. The first pattern is observed in three experiments at 40(2) GPa, 51(3) GPa and 93(7) GPa and is consistent with hexagonal symmetry. As an example, diffraction data for Si at 51(3) GPa (Figs. 2(a) and (c)) is compared with simulated hcp, dhcp and sh structures with best-fit lattice parameters. This experimental lineout agrees well with hcp

structure with $a_{\text{hep}} = 2.490(5) \text{ Å}, c_{\text{hep}} = 4.199(11) \text{ Å},$ and $\rho_{\rm hep} = 4.14(2)\,{\rm g/cm^3}$. The dhcp structure, predicted by theory [17–19], is another strong contender, whose lattice parameters are fit to $a_{\text{dhep}} = 2.481(5) \text{ Å}$, $c_{\rm dhep} = 8.49(2) \,\text{Å}$, and $\rho_{\rm dhep} = 4.12(2) \,\text{g/cm}^3$. However, the (103) peak is absent across the entire azimuth in our observation. Though somewhat textured, the (104) peak is observed, despite being predicted to be of lower intensity than (103) peak in the simulation. The texture of the (104) peak observed does not allow the absence of (103) peak across the $\sim 300^{\circ}$ observable azimuth angle in these experiments. This provides enough evidence against the existence of a dhcp structure at this condition. The simulated pattern for sh, using the hcp lattice parameters, agrees well with the data albeit with some minor differences. However, there are two arguments against the sh structure. The first being that the unit cell of sh structure contains only one atom, as opposed to two atoms in the case of hcp, which indicates that the density is only half of what can be expected from the isentrope calculated using DFT [30] (Figure 3(b)). The second argument is that the axial ratio c/a is 1.687(5), almost twice as big as the theoretical value of 0.942 at 29 GPa and 0 K [18]. The sh structure is not close-packed like hcp or dhcp, and we expect its c/a to be close to 1. These two arguments rule out the sh as a candidate for the observed structure. We therefore interpret the structure as hcp, with a weighted average c/a = 1.6861(9).

The second pattern is observed between 153 and 389 GPa, in seven different shots. Diffraction data for Si at 389(11) GPa (Figure 2(b) and (d)) show the characteristic fcc (111) and (200) peaks. The expected location of the third peak (220) for fcc calculated using the best-fit $a_{\rm fcc} = 2.996(8)$ Å would be $2\theta = 88.747^{\circ}$, which partially overlaps with the pinhole (013) peak (Figure 2(d)).

The measured d-spacings are compared to values calculated with density along the DFT isentrope [30] (Figure 3(a)). The DFT calculation [18, 19] predicts the dhcp phase along the DFT isentrope above 22 GPa, transitioning to fcc above 55 GPa [18, 30] (Figure 4(a)). In contrast, our data show that the hcp stability region extends above the isentrope over a pressure from at least 40 to 93 GPa, with a transition to fcc between 93 and 153 GPa. The data also confirm that the fcc phase is stable to at least 389 GPa, in agreement with the DFT calculation [18, 19].

The observation of the hcp phase along the ramp compression path between 40 and 93 GPa corroborates the results of a shock compression experiment[16]. Their data (Figure 4(b)) suggest the existence of a sh-hcp-liquid triple point, and a direct phase boundary between the sh and hcp phases without the predicted dhcp phase inbetween. The onset of the sh-hcp transition in [16] is close to the phase space assigned to be hcp by our data (red shaded in Figure 4(b)). The DAC data at ambient temperature and our ramp data together suggest a positive

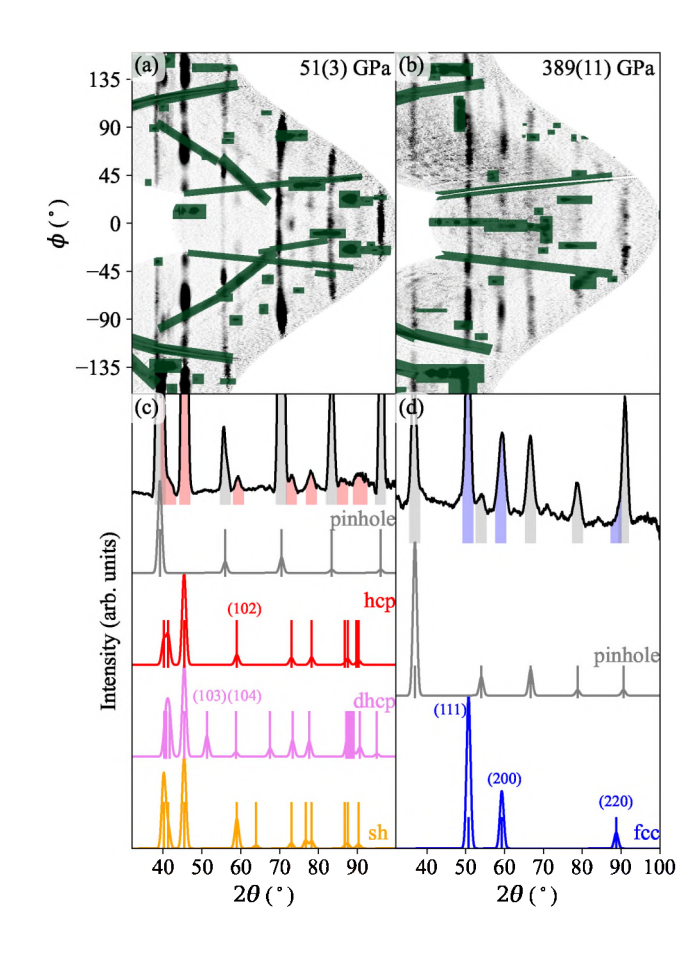
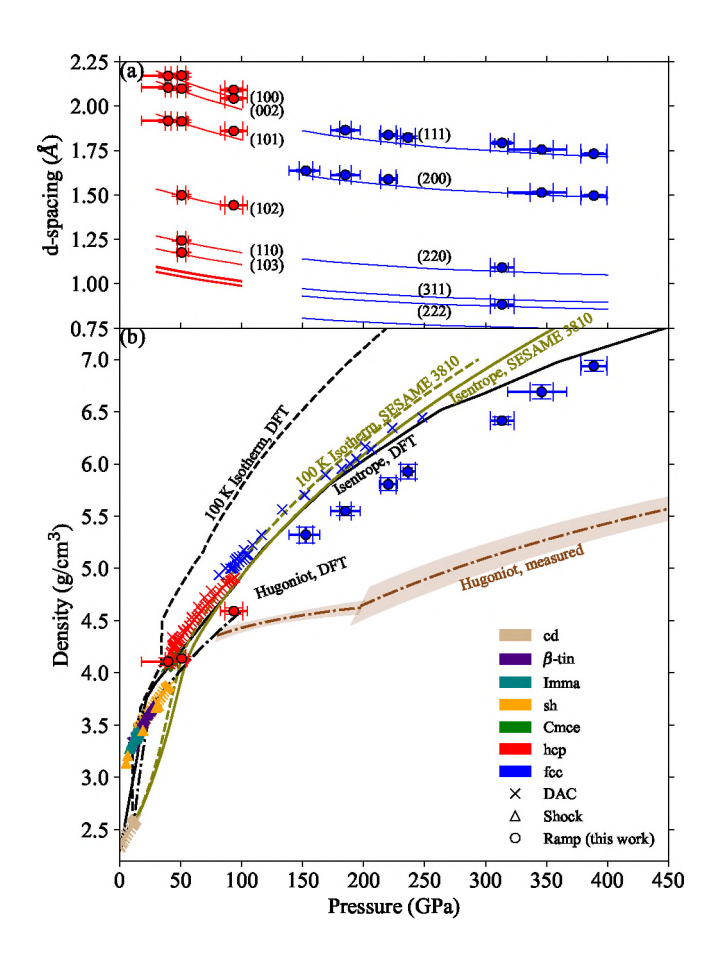


FIG. 2. X-ray diffraction measurements of Si at (a) 51(3) GPa and (b) 389(11) GPa, respectively. Rectangular image plates are digitally projected onto a $2\theta-\phi$ plane, where 2θ is the scattering angle and ϕ is the azimuthal angle around $2\theta=0$. Features not originating from the compressed Si sample or pinhole are masked out (green shade) when taking the lineout of images (see supplementary materials). (c) An azimuthally averaged lineout (black) of the diffraction image in (a) is compared with simulated diffraction patterns of three candidate structures, whose ideal peak locations are marked by vertical lines. Ideal peak positions from the pinhole material used for image plate calibration are shaded by gray, and peaks from the sample are shaded in red. (d) Lineout of the diffraction image in (b) is compared with the simulated fcc structure. Peaks from the sample are shaded in blue.

slope for the hcp-fcc phase boundary.

We discovered a significant increase in stability of the hcp structure for dynamically compressed silicon at pressures and temperatures where dhcp or fcc phases are predicted. Two potential explanations for this, include (1) the hcp phase is energetically favored, or (2) the hcp phase is somehow stabilized by the dynamic compression techniques used in this work, such as the presence of deviatoric stresses. It has been observed that phase diagrams measured in dynamic compression experiments can differ from those from hydrostatic DAC experiments. For ex-



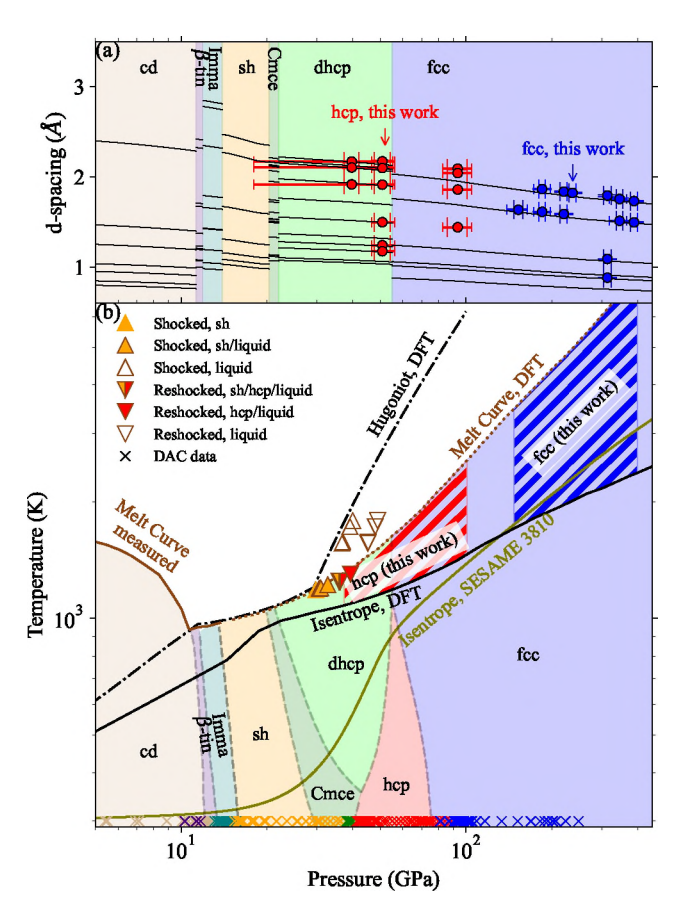


FIG. 3. (a) Pressure dependence of the measured d-spacings. The structure between 40 and 93 GPa is interpreted as hcp, and that between 153 and 390 GPa as fcc. The solid lines represent d-spacings of hcp (red) and fcc (blue) structures calculated using the DFT isentrope [30]. (b) Density-pressure phase diagram data of Si. Data of this work are shown in circles, DAC data [1–9] as crosses, and shock data [14–16] as triangles. For this work, the 1σ uncertainty in the mean pressure and the 1σ interval of the pressure distribution at the time of exposure are shown with larger and smaller caps on the error bars. Various curves are shown: 100 K isotherm and principal isentrope from SESAME 3810 table, 100 K isotherm, principal Hugoniot [19] and principal isentrope [30] from DFT calculation, and measured Hugoniot [34]. Our data show lower densities than both DFT and SESAME isentropes.

ample, a lowering of the cd- β tin-Imma phase boundaries in Si has been reported in dynamic compression experiments [14]. Also, it was observed that diamond remains in its ambient phase (FC8) up to 2 TPa under ramp compression, despite being predicted to transform into BC8 at 1 TPa [31]. Finally, the dhcp phase was observed at 5-20 GPa near the melting boundary in DAC experiments [32] but not in dynamic compression experiments [33].

The densities calculated using the measured lattice parameters are higher than those along the measured Hugoniot [34] as expected, but systematically lower than

FIG. 4. (a) Pressure dependence of d-spacing for all phases along the DFT isentrope [30], shown as solid lines. Data of this work show hcp structure from 40 GPa up to at least 93 GPa, with first evidence of fcc at 153 GPa. The phases predicted by DFT are shaded with their respective colors. Along the isentrope, theory predicts dhep structure between 22 and 55 GPa, and fcc structure above 55 GPa. The Imma and Cmce phases are of very low symmetries and a 10% intensity threshold is applied to them to reduce the number of lines. (b) The pressure-temperature phase diagram [35]. The solidsolid phase boundaries, calculated using DFT [18, 19], are shown as dashed curves. DFT isentrope [30], SESAME-3810 isentrope, DFT Hugoniot [18], and melt curve [18] are also shown. Data of this work fall between the theoretical principal isentrope and the melt curve, indicated by striped red and blue regions for observed hcp and fcc structures, respectively. Shock data and reshock data [16] of various phases are shown. The reshocked states at 35.8 GPa and 36.2 GPa are sh/hcp/liquid mixtures, and the reshocked state at 39.3 GPa is hcp/liquid mixture. These data show good agreement with this work.

the DFT isentrope [30] and the SESAME 3810 isentrope (Figure 3(b)). Due to the elastic-plastic transition, first-order phase transitions of the constituent target materials, and limitations in pulse shaping capabilities, the compression path contains multiple weak shocks [36] that increase the sample temperature compared to

the principal isentrope. Though temperature is not measured, the DFT isentrope and melt curve give a reasonable constraint on it (Figure 4(b)). On the other hand, the SESAME and DFT isentropes are not guaranteed to be correct. This is evident from that the $T=100\,\mathrm{K}$ isotherm from the same DFT calculation [19], while correctly capturing the density jumps at cd- β tin and sh-hcp transitions, overpredicts density compared to the DAC data at ambient temperature [1, 6–9] by about 15%. The $T=100\,\mathrm{K}$ SESAME isotherm is closer to DAC measurement at pressures higher than 50 GPa, but does not capture the density jumps at lower pressures. The same inaccuracy can happen along isentropes as well.

In conclusion, powder x-ray diffraction was used to measure crystal structure of Si between 40 and 389 GPa along a thermodynamic path close to the principal isentrope. Along this path, the hcp structure is stable to at least 93 GPa, a much higher pressure than predicted by simulations, and the fcc phase is stable from 153 GPa to at least 389 GPa. Data show no evidence for the predicted dhcp phase. This is likely due to that the hcp phase is more energetically favored, or the nonhydrostaticity of the loading path. These observations show that Si exhibits interesting and unexpected behavior under ramp loading not captured by theoretical calculations, motivating improved DFT calculations for equilibrium phase diagrams, and Molecular Dynamics simulations for phase transition pathways and kinetics [37].

The authors thank the OMEGA EP team for laser operation and diagnostic support. We thank T. Cracium and the LLE target fabrication team. We thank Jon H. Eggert and Marius Millot at Lawrence Livermore National Laboratory for the permission to use Analyze-VISAR and AnalyzePXRDIP analysis software packages. This material was based upon work supported by the Department of Energy National Nuclear Security Administration under Award No. DE-NA0003856, the University of Rochester, and the New York State Energy Research and Development Authority. A portion of this work was performed under the auspices of the U.S. Department of Energy by Lawrence Livermore National Laboratory under Contract No. DE-AC52-07NA27344. for this research is provided in part by the Center for Matter at Atomic Pressures (CMAP), a National Science Foundation (NSF) Physics Frontiers Center, under Award PHY-2020249.

This report was prepared as an account of work sponsored by an agency of the U.S. Government. Neither the U.S. Government nor any agency thereof, nor any of their employees, makes any warranty, express or implied, or assumes any legal liability or responsibility for the accuracy, completeness, or usefulness of any information, apparatus, product, or process disclosed, or represents that its use would not infringe privately owned rights. Reference herein to any specific commercial product, process, or service by trade name, trademark, manufacturer,

or otherwise does not necessarily constitute or imply its endorsement, recommendation, or favoring by the U.S. Government or any agency thereof. The views and opinions of authors expressed herein do not necessarily state or reflect those of the U.S. Government or any agency thereof.

- * xgon@lle.rochester.edu
- S. Anzellini, M. T. Wharmby, F. Miozzi, A. Kleppe,
 D. Daisenberger, and H. Wilhelm, Scientific Reports 9, 10.1038/s41598-019-51931-1 (2019).
- [2] J. Z. Hu, L. D. Merkle, C. S. Menoni, and I. L. Spain, Physical Review B 34, 4679 (1986).
- [3] J. C. Jamieson, Science **139**, 762 (1963).
- [4] M. I. McMahon and R. J. Nelmes, Physical Review B 47, 8337 (1993).
- [5] M. I. McMahon, R. J. Nelmes, N. G. Wright, and D. R. Allan, Physical Review B 50, 739 (1994).
- [6] H. Olijnyk, S. Sikka, and W. Holzapfel, Physics Letters A 103, 137 (1984).
- [7] M. Hanfland, U. Schwarz, K. Syassen, and K. Takemura, Physical Review Letters 82, 1197 (1999).
- [8] S. J. Duclos, Y. K. Vohra, and A. L. Ruoff, Physical Review Letters 58, 775 (1987).
- [9] S. J. Duclos, Y. K. Vohra, and A. L. Ruoff, Physical Review B 41, 12021 (1990).
- [10] M. N. Pavlovskii, Fiz. Tverd. Tela 9, 3192 (1967).
- [11] W. H. Gust and E. B. Royce, Journal of Applied Physics 42, 1897 (1971).
- [12] T. Goto, T. Sato, and Y. Syono, Japanese Journal of Applied Physics 21, L369 (1982).
- [13] S. J. Turneaure and Y. M. Gupta, Applied Physics Letters 91, 201913 (2007).
- [14] E. E. McBride, A. Krygier, A. Ehnes, E. Galtier, M. Harmand, Z. Konôpková, H. J. Lee, H.-P. Liermann, B. Nagler, A. Pelka, M. Rödel, A. Schropp, R. F. Smith, C. Spindloe, D. Swift, F. Tavella, S. Toleikis, T. Tschentscher, J. S. Wark, and A. Higginbotham, Nature Physics 15, 89 (2018).
- [15] S. J. Turneaure, N. Sinclair, and Y. M. Gupta, Phys. Rev. Lett. 117, 045502 (2016).
- [16] S. J. Turneaure, S. M. Sharma, and Y. Gupta, Physical Review Letters 121, 10.1103/physrevlett.121.135701 (2018).
- [17] C. Li, C. Wang, J. Han, L. Yan, B. Deng, and X. Liu, Journal of Materials Science 53, 7475 (2018).
- [18] R. Paul, S. Hu, and V. Karasiev, Physical Review Letters 122, 10.1103/physrevlett.122.125701 (2019).
- [19] R. Paul, S. X. Hu, and V. V. Karasiev, Phys. Rev. B 100, 144101 (2019).
- [20] J. R. Rygg, J. H. Eggert, A. E. Lazicki, F. Coppari, J. A. Hawreliak, D. G. Hicks, R. F. Smith, C. M. Sorce, T. M. Uphaus, B. Yaakobi, and G. W. Collins, Review of Scientific Instruments 83, 113904 (2012).
- [21] F. Coppari, R. F. Smith, D. B. Thorn, J. R. Rygg, D. A. Liedahl, R. G. Kraus, A. Lazicki, M. Millot, and J. H. Eggert, Review of Scientific Instruments 90, 125113 (2019).
- [22] P. M. Celliers, D. K. Bradley, G. W. Collins, D. G. Hicks, T. R. Boehly, and W. J. Armstrong, Review of Scientific Instruments 75, 4916 (2004).

- [23] L. E. Kirsch, S. J. Ali, D. E. Fratanduono, R. G. Kraus, D. G. Braun, A. Fernandez-Pañella, R. F. Smith, J. M. McNaney, and J. H. Eggert, Journal of Applied Physics 125, 175901 (2019).
- [24] J. R. Maw, in AIP Conference Proceedings (AIP, 2004).
- [25] S. D. Rothman and J. Maw, Journal de Physique IV (Proceedings) 134, 745 (2006).
- [26] J. T. Larsen and S. M. Lane, Journal of Quantitative Spectroscopy and Radiative Transfer 51, 179 (1994).
- [27] J. K. Wicks, R. F. Smith, D. E. Fratanduono, F. Coppari, R. G. Kraus, M. G. Newman, J. R. Rygg, J. H. Eggert, and T. S. Duffy, Science Advances 4, eaao5864 (2018).
- [28] C. T. Seagle, J.-P. Davis, and M. D. Knudson, Journal of Applied Physics 120, 165902 (2016), https://doi.org/10.1063/1.4965990.
- [29] J. R. Rygg, R. F. Smith, A. E. Lazicki, D. G. Braun, D. E. Fratanduono, R. G. Kraus, J. M. McNaney, D. C. Swift, C. E. Wehrenberg, F. Coppari, M. F. Ahmed, M. A. Barrios, K. J. M. Blobaum, G. W. Collins, A. L. Cook, P. D. Nicola, E. G. Dzenitis, S. Gonzales, B. F. Heidl, M. Hohenberger, A. House, N. Izumi, D. H. Kalantar, S. F. Khan, T. R. Kohut, C. Kumar, N. D. Masters, D. N. Polsin, S. P. Regan, C. A. Smith, R. M. Vignes, M. A. Wall, J. Ward, J. S. Wark, T. L. Zobrist, A. Arsenlis, and J. H. Eggert, Review of Scientific Instruments 91, 043902 (2020).
- [30] R. Paul, Private communication (2022).
- [31] A. Lazicki, D. McGonegle, J. R. Rygg, D. G. Braun, D. C. Swift, M. G. Gorman, R. F. Smith, P. G. Heigh-

- way, A. Higginbotham, M. J. Suggit, D. E. Fratanduono, F. Coppari, C. E. Wehrenberg, R. G. Kraus, D. Erskine, J. V. Bernier, J. M. McNaney, R. E. Rudd, G. W. Collins, J. H. Eggert, and J. S. Wark, Nature **589**, 532 (2021).
- [32] D. Errandonea, Y. Meng, D. H. usermann, and T. Uchida, Journal of Physics: Condensed Matter 15, 1277 (2003).
- [33] M. T. Beason, A. Mandal, and B. J. Jensen, Physical Review B 101, 024110 (2020).
- [34] B. J. Henderson, M. C. Marshall, T. R. Boehly, R. Paul, C. A. McCoy, S. X. Hu, D. N. Polsin, L. E. Crandall, M. F. Huff, D. A. Chin, J. J. Ruby, X. Gong, D. E. Fratanduono, J. H. Eggert, J. R. Rygg, and G. W. Collins, Physical Review B 103, 10:1103/physrevb.103.094115 (2021).
- [35] See Supplementary Material Section 5 for a further discussion of the phase diagram, which includes [6, 7, 9, 17, 18, 29, 31, 38].
- [36] D. E. Fratanduono, R. F. Smith, D. G. Braun, J. R. Patterson, R. G. Kraus, T. S. Perry, A. Arsenlis, G. W. Collins, and J. H. Eggert, Journal of Applied Physics 117, 245903 (2015).
- [37] L. He, D. Polsin, S. Zhang, G. W. Collins, and N. Abdolrahim, Scientific Reports 12, 10.1038/s41598-022-23785-7 (2022).
- [38] Y. K. Vohra, K. E. Brister, S. Desgreniers, A. L. Ruoff, K. J. Chang, and M. L. Cohen, Physical Review Letters 56, 1944 (1986).